Supplementary Materials

Piezochromic metal-organic framework films for interfacial pressure mapping

Lin Zheng[1,#], Jinhui Gu[1,#], Junshuai Chen[1], Jun-Zhe Dong[1], Jia-Sen Xie[1], Ying Yang[1], Mingwei Gu[1], Xingyu Ma[1], Mengxing Huang[1], Jin Ge[1,*], Mei Pan[1,2,*], Cheng-Yong Su[1,*]

[1]GBRCE for Functional Molecular Engineering, LIFM, IGCME, School of Chemistry, Sun Yat-Sen University, Guangzhou 510275, Guangdong, China.
[2]State Key Laboratory of Chemistry and Utilization of Carbon Based Energy Resources, College of Chemistry, Xinjiang University, Urumqi 830046, Xinjiang, China.
[#]These authors contributed equally to this work.

[*]**Correspondence to:** Prof. Cheng-Yong Su, Prof. Mei Pan, Prof. Jin Ge, GBRCE for Functional Molecular Engineering, LIFM, IGCME, School of Chemistry, Sun Yat-Sen University, Guangzhou 510006, Guangdong, China. E-mail: cesscy@mail.sysu.edu.cn; panm@mail.sysu.edu.cn; gejin@mail.sysu.edu.cn

Calculation method for film color uniformity evaluation

The input image was first converted from the RGB color space to the CIELAB color space. For an image of size $M \times N$, each pixel is represented as a three-dimensional color vector (L^*, a^*, b^*). By unfolding all pixels, a color data matrix was constructed as:

$$X=\begin{bmatrix} L_1^* & a_1^* & b_1^* \\ \vdots & \vdots & \vdots \\ L_n^* & L_n^* & L_n^* \end{bmatrix} \in R^{n\times 3}$$

where $n=M\times N$ denotes the total number of pixels.

The mean color vector in the CIELAB space was then computed as:

$$\mu = [\mu_L \quad \mu_a \quad \mu_b]$$

with

$$\mu_L = \frac{1}{n}\sum_{i=1}^{n} L_i^*, \qquad \mu_a = \frac{1}{n}\sum_{i=1}^{n} a_i^*, \qquad \mu_b = \frac{1}{n}\sum_{i=1}^{n} b_i^*$$

The mean vector represents the global color position of the image in the perceptually uniform CIELAB space.

The covariance matrix of the color distribution was then constructed as:

$$\mathrm{C} = \frac{1}{n-1}\mathrm{X}^{\mathrm{T}}\mathrm{X}$$

which can be explicitly expressed in terms of variance and covariance components as:

$$\mathrm{C} = \begin{bmatrix} Var(L^*) & Cov(L^*, a^*) & Cov(L^*, b^*) \\ Cov(L^*, a^*) & Var(a^*) & Cov(a^*, b^*) \\ Cov(L^*, b^*) & Cov(a^*, b^*) & Var(b^*) \end{bmatrix}$$

with

$$Var(L^*) = \frac{1}{n-1}\sum_{k=1}^{n}(L_k^* - \mu_L)^2$$

$$Cov(L^*, a^*) = \frac{1}{n-1}\sum_{k=1}^{n}(L_k^* - \mu_L)(a_k^* - \mu_a)$$

and analogous definitions apply to all remaining diagonal and off-diagonal terms. The diagonal entries quantify the intrinsic dispersion of each color channel, whereas the off-diagonal terms describe cross-correlations between different channels.

Since the covariance matrix is real and symmetric, it can be diagonalized via eigenvalue decomposition:

$$\mathrm{C}v_i = \lambda_i v_i$$

where λ_i and v_i denote the eigenvalues and eigenvectors, respectively. The eigenvalues are obtained by solving:

$$\det(\mathrm{C} - \lambda \mathrm{I}) = 0$$

yielding three real eigenvalues:

$$\lambda_1 \geq \lambda_2 \geq \lambda_3$$

and the corresponding eigenvectors form an orthonormal basis:

$\mathrm{V} = [v_1, v_2, v_3]$

Geometrically, the eigenvectors define the principal axes of the color distribution in the

CIELAB space, while the eigenvalues quantify the variance of the data along these directions. A larger eigenvalue indicates a broader distribution of colors along the corresponding principal direction, whereas a smaller eigenvalue indicates a more concentrated distribution.

To provide a scalar metric for overall color dispersion, a representative eigenvalue was defined as the arithmetic mean of the three eigenvalues:

$$\lambda_{rep} = \frac{\lambda_1 + \lambda_2 + \lambda_3}{3}$$

Given that the trace of the covariance matrix satisfies:

$$tr(\mathrm{C}) = \lambda_1 + \lambda_2 + \lambda_3$$

the representative eigenvalue can be equivalently written as:

$$\lambda_{rep} = \frac{tr(\mathrm{C})}{3}$$

This metric reflects the average variance of the color distribution in the principal directions and thus serves as a robust descriptor of overall color heterogeneity.

In this framework, λ_{rep} provides a quantitative measure of color uniformity: lower values correspond to tightly clustered color distributions and higher color uniformity, whereas larger values indicate increased color dispersion and reduced uniformity. Therefore, the representative eigenvalue can be interpreted as an inverse metric of color homogeneity, enabling quantitative evaluation of spatial color variation in functional materials.

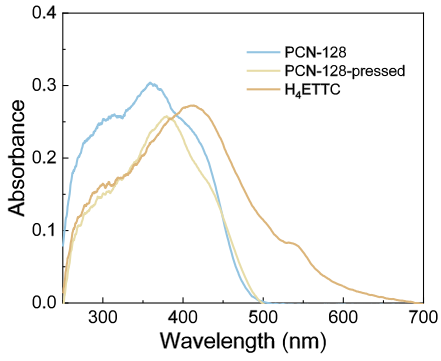

Supplementary Figure 1. Ultraviolet-visible absorption spectroscopy (UV-Vis) of

PCN-128, PCN-128-pressed, and H_4ETTC.

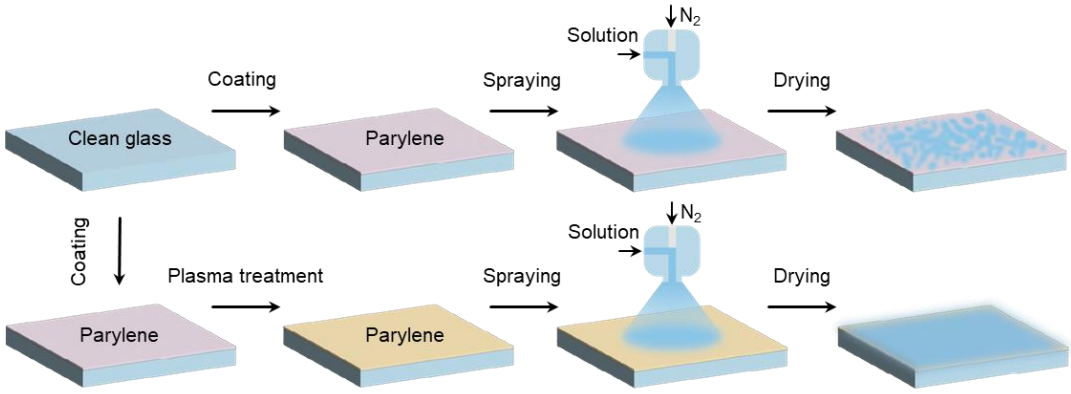

Supplementary Figure 2. Schematic diagram of the PCN-128 film spraying process**.**

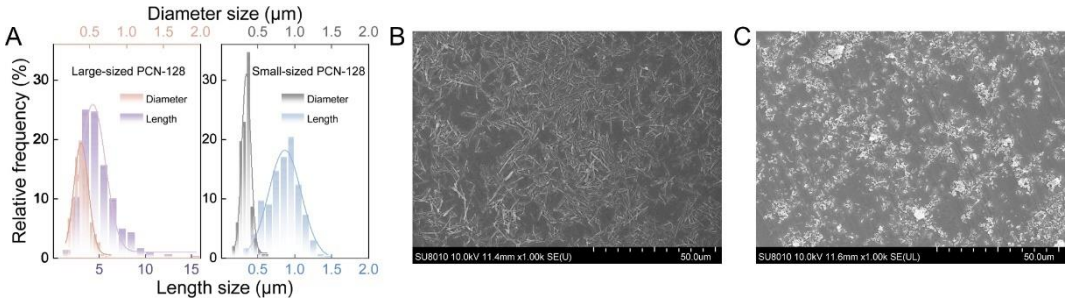

Supplementary Figure 3. (A) Particle size distributions of large- (B) and small-sized (C) PCN-128 samples were determined by measuring 300 particles from SEM images.

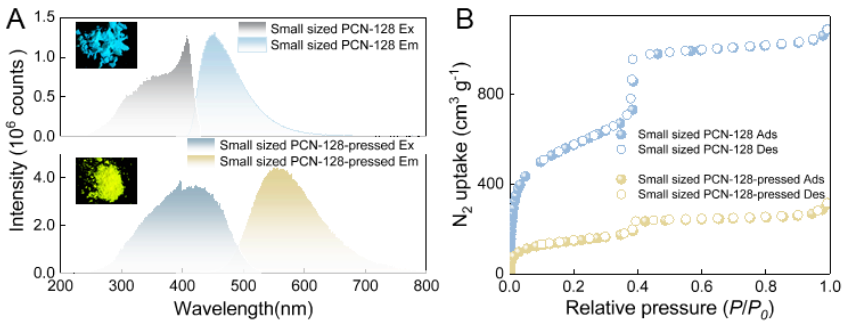

Supplementary Figure 4. Fluorescence spectrum (A) and N_2 adsorption isotherms (B) of small sized PCN-128.

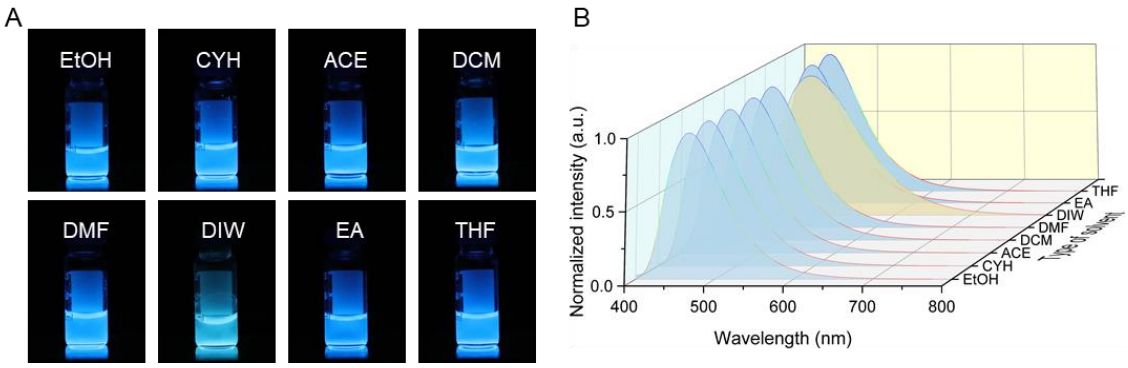

Supplementary Figure 5. Images (A) and emission spectrum (excitation: 365 nm) (B) of large sized PCN-128 in various solvents (EtOH: ethanol, CYH: cyclohexane, ACE: acetone, DCM: dichloromethane, DMF: N,N-Dimethylformamide, DIW: deionized water, EA: ethyl acetate, THF: tetrahydrofuran).

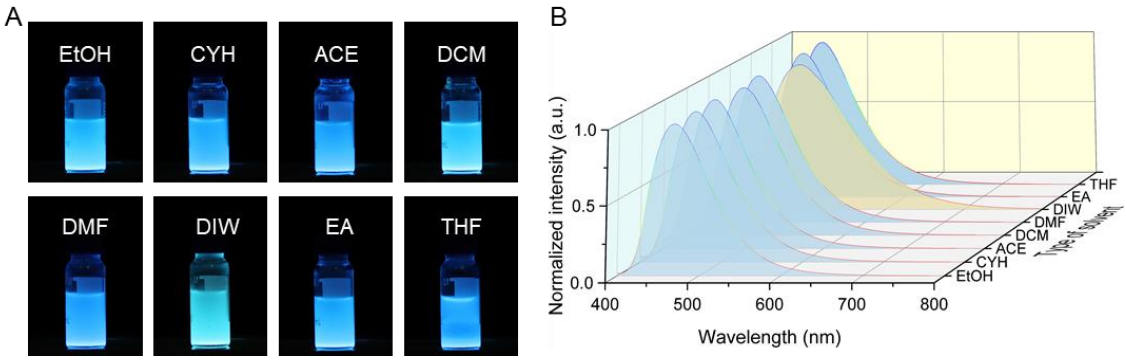

Supplementary Figure 6. Images (A) and emission spectrum (excitation: 365 nm) (B) of small sized PCN-128 in various solvents (EtOH: ethanol, CYH: cyclohexane, ACE: acetone, DCM: dichloromethane, DMF: N,N-Dimethylformamide, DIW: deionized water, EA: ethyl acetate, THF: tetrahydrofuran).

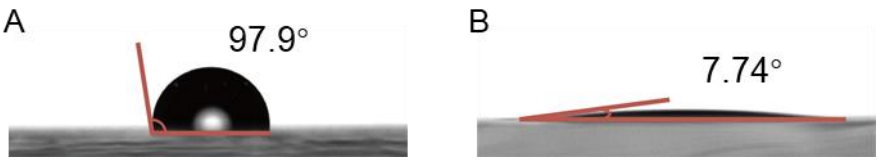

Supplementary Figure 7. Water contact angle of parylene substrates before (A) and after (B) hydrophilic treatment.

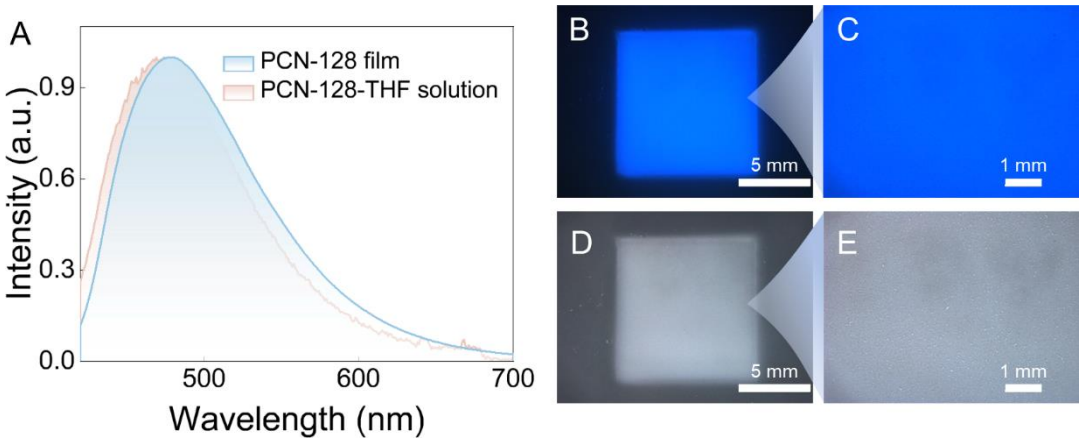

Supplementary Figure 8. Emission spectrum (excitation: 365 nm) (A). Images of PCN-128 film under UV (B-C) and ambient light (D-E).

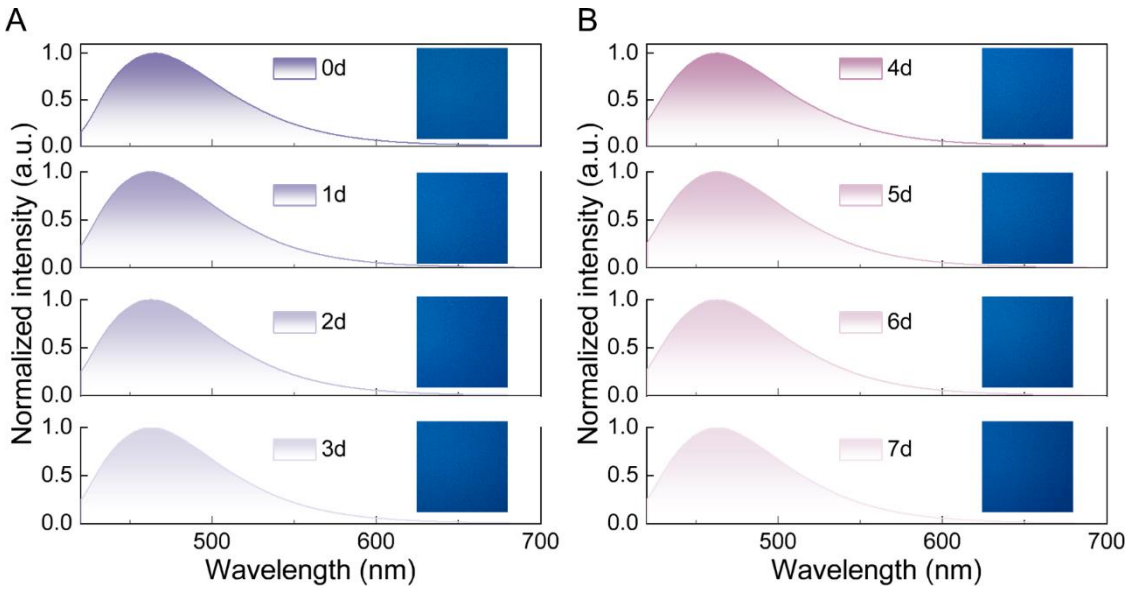

Supplementary Figure 9. (A, B) Photographs and emission spectra of PCN-128 films continuously monitored for 7 days under ultraviolet light.

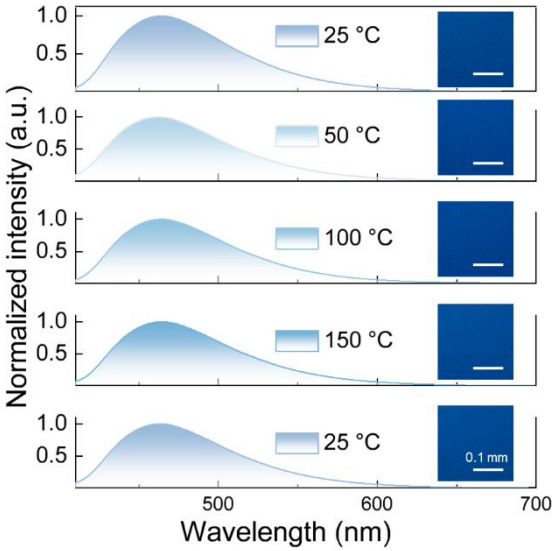

Supplementary Figure 10. Photographs and corresponding spectra of PCN-128 film at 25, 50, 100, 150, and 25 °C (excitation: 365 nm).

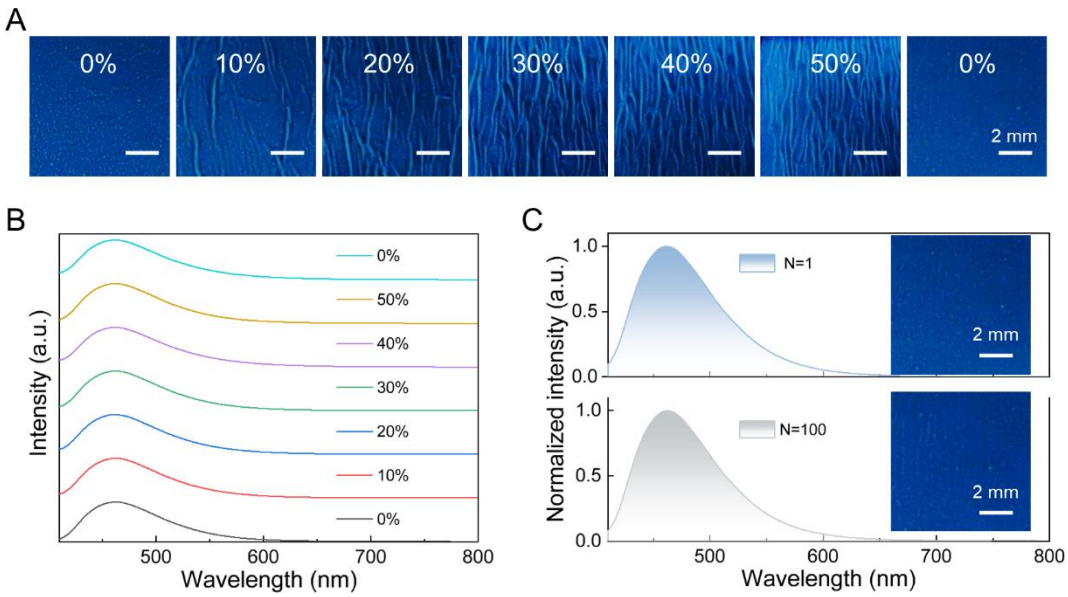

Supplementary Figure 11. (A) Photographs and (B) spectra under various compression states (excitation: 365 nm). (C) Photographs and spectra after 100 compression-relaxation cycles at 50% strain (excitation: 365 nm).

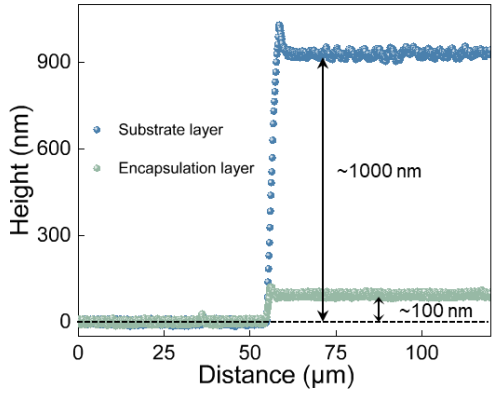

Supplementary Figure 12. Thickness of the parylene substrate and encapsulation layer.

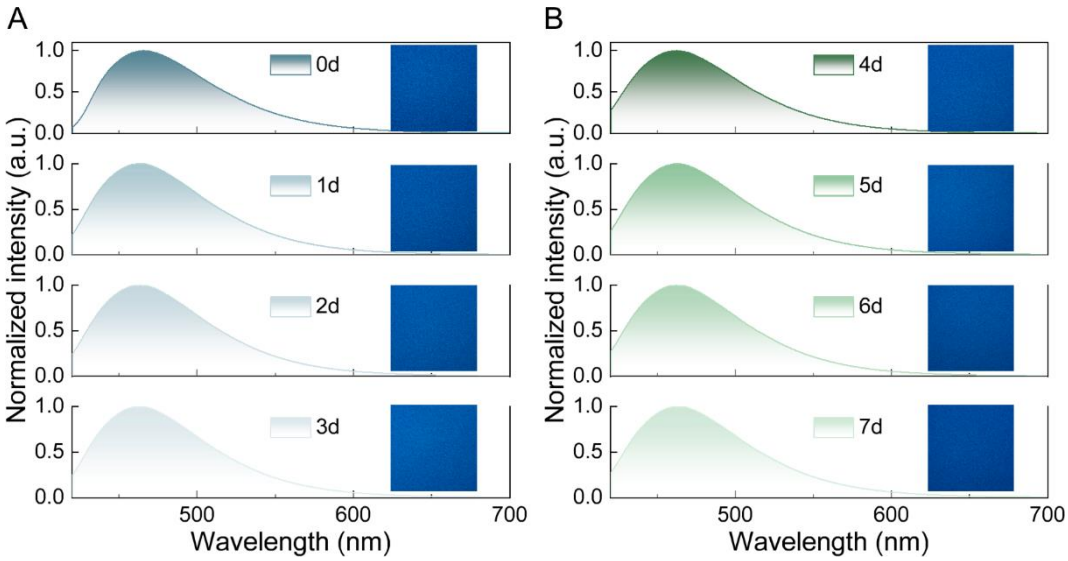

Supplementary Figure 13. (A, B) Photographs and emission spectra of PCN-128 films continuously monitored for 7 days at room temperature under a relative humidity (RH) of 90%.

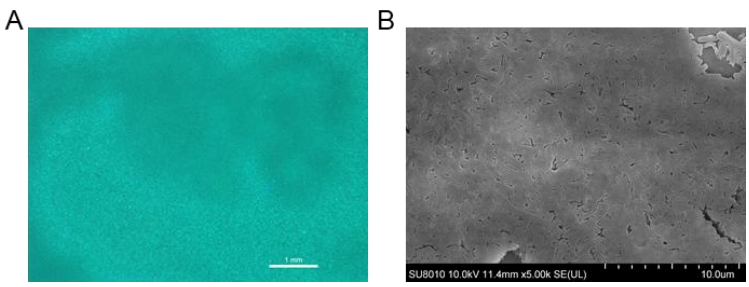

Supplementary Figure 14. Optical image (A) (under UV) and SEM image (B) of PCN-128 film after compression.

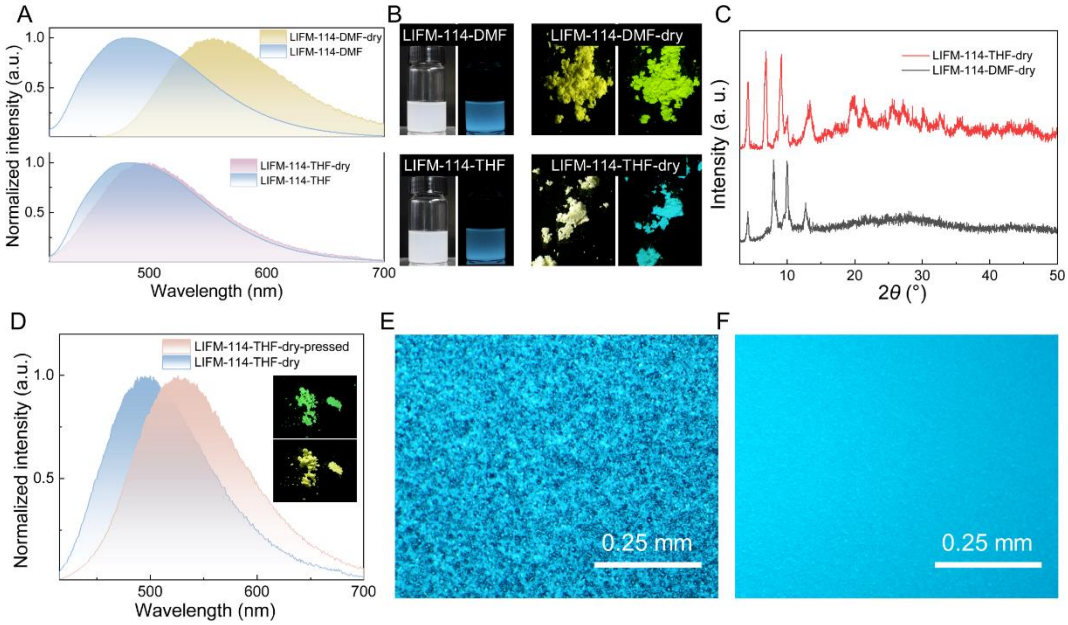

Supplementary Figure 15. (A, B) Photographs and emission spectra of LIFM-114 in DMF and THF solvent environments, together with the corresponding images and emission spectra after solvent removal. (C) PXRD patterns of LIFM-114 after solvent removal from DMF and THF. (D) Photographs and emission spectra of LIFM-114 dried from THF after mechanical compression. Optical images of spray-coated LIFM-114 films fabricated on substrates (E) before and (F) after wettability modification.

To evaluate the applicability of the solvent exchange and wettability regulation strategies beyond PCN-128, we synthesized LIFM-114[1] and systematically investigated its structural evolution and luminescence response during drying in different solvents. LIFM-114 exhibited light-green emission in the solvent state. After drying in DMF, its emission color shifted from yellow-green to yellow, accompanied by the loss of its original optical response. In contrast, LIFM-114 retained its initial emission color after drying in THF. PXRD analysis further confirmed that the solvent-induced color variation originated from structural transformation of the framework.

Although framework breathing endows MOFs with diverse stimulus-responsive properties, it may also compromise the stability and controllability of piezochromic responses. Therefore, the solvent exchange strategy developed in this work provides an effective approach for preserving the structural integrity and optical stability of flexible

MOF systems during thin-film fabrication. Furthermore, during the fabrication of LIFM-114 films, wettability-modified substrates promoted uniform crystal spreading, resulting in continuous films with homogeneous crystal distribution. These results further demonstrate that substrate wettability engineering represents an effective and general strategy for constructing high-quality MOF thin films.

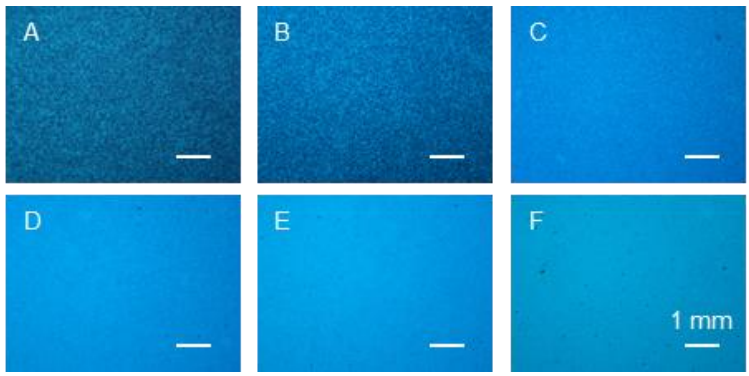

Supplementary Figure 16. (A-F) Optical images of the film with various surface loading of PCN-128 (0.8, 1.6, 2.4, 3.2, 4.0, 4.8 mg cm^{-2}). (Scale bars: 1 mm)

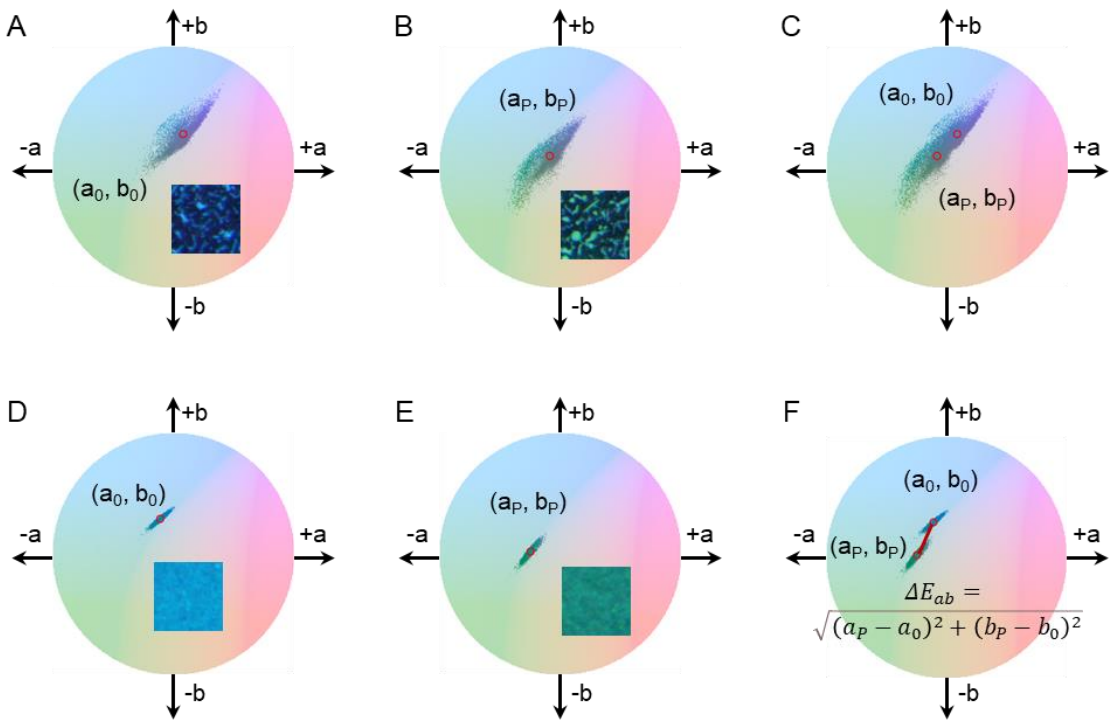

Supplementary Figure 17. Chromaticity distribution of PCN-128 film with non-color uniformity in the a-b color space before (A) and after (B) compression. Chromaticity distribution of PCN-128 film with high color uniformity in the ab color space before (D) and after (E) compression. A comparison of the color difference (ΔE_{ab}) between

non-uniform (C) and uniform (F) PCN-128 films before and after compression revealed that the color distribution of the color uniform films showed a clear distinction before and after compression, resulting in more accurate pressure detection.

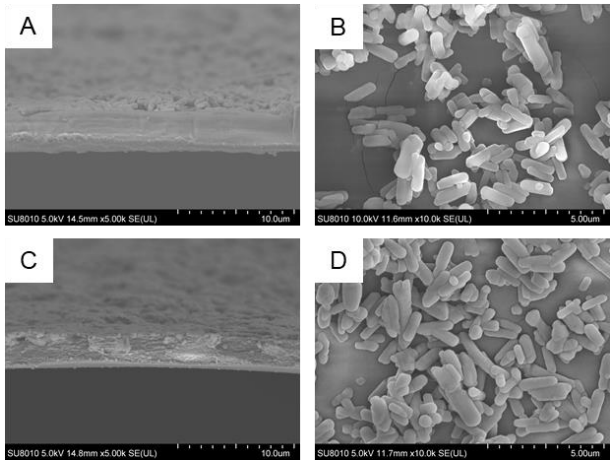

Supplementary Figure 18. Cross-sectional and surface SEM images of the films with different surface loading of PCN-128 (A-B: 1.6 mg cm^{-2}, C-D: 4.8 mg cm^{-2}).

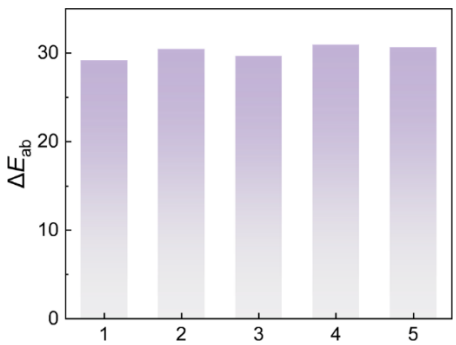

Supplementary Figure 19. Evaluation of batch-to-batch signal reproducibility for PCN-128 films (PCN-128 loading: 4.8 mg cm^{-2}, pressure: 101.86 MPa).

Supplementary Figure 20. Different grits (320-, 600-, 800-, 1000-, and 3000-grit sandpaper) of sandpaper imprint images of PCN-128 film (Scale bars: 500 μm).

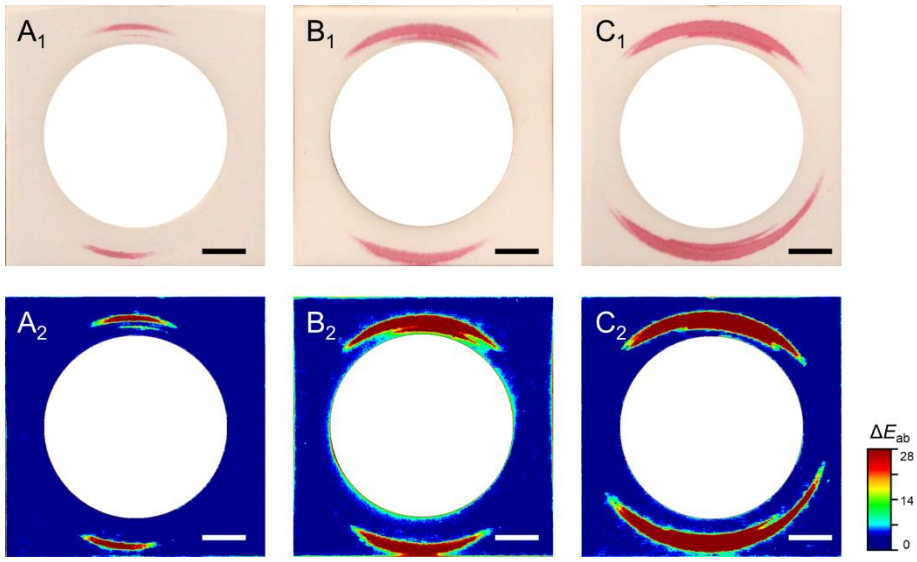

Supplementary Figure 21. Commercial Fuji film images (A_1, B_1, C_1) and ΔE_{ab} maps (A_2, B_2, C_2) of the interface pressure testing process for threaded fasteners (Scale bars: 1 cm).

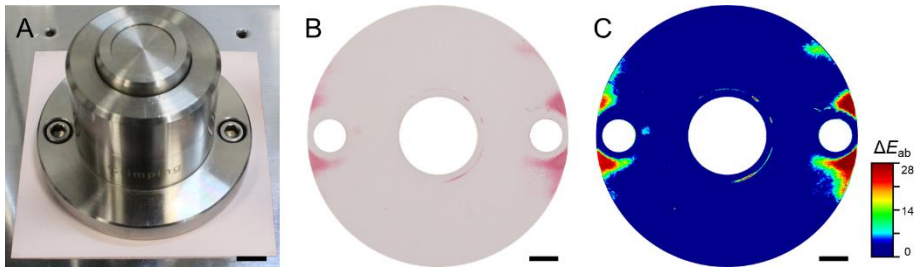

Supplementary Figure 22. Interface pressure detection for the assembly of large-scale fasteners with commercial Fuji film (Scale bars: 5 mm).

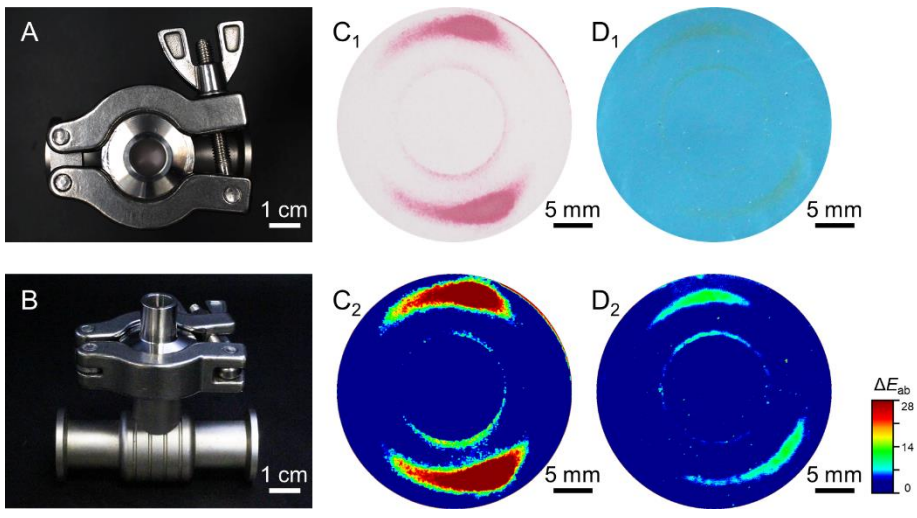

Supplementary Figure 23. Interfacial stress monitoring of a vacuum clamp using piezochromic films. (A, B) Photographic view of the vacuum clamp; Interfacial stress

distribution maps captured by (C_1, C_2) the commercial Fuji film and (D_1, D_2) the PCN-128 film.

Supplementary Table 1. Comparison with previously reported piezochromic films

Piezochromic material	**Sensing range (MPa)**	**Sensitivity (MPa^{-1})**	**Uniformity calculation**	**Large-scale fabrication**	**Color retention**	**Ref**
ZnS:Mn	0.0006-0.2, and 0.65-30	6, and 0.037	O	O	O	[2]
Thermochromic composite	0.4-0.73	/	O	O	O	[3]
ZnS:Cu	0.00125-0.04	/	O	P	O	[4]
ZnS:Cu	0.01-2.4	0.19	O	O	O	[5]
InGaN/GaN multiple quantum well	1.87-14.94	0.03909	O	O	O	[6]
Triboelectric sensor	0.001-0.15	60	O	O	O	[7]
Triboelectric sensor	0-0.08	/	O	O	O	[8]
Electroluminescent skin	0-0.4	5000000	O	O	O	[9]
Multipoint 3-axis pressure sensor	0-0.36	/	O	O	O	[10]
MoS_2 Transistors	0.0002-5	0.018, and 1.8	O	O	O	[11]
Indium gallium zinc oxide thin film transistors	0-0.4	1.16	O	O	O	[12]
CdS	0-100	/	O	O	O	[13]

Luminescent e-skin	0-0.18	0.011	O	O	O	[14]
PCN-128	**5.09-101.86, and 7.33-178.25**	**0.92, and 0.30**	**P**	**P**	**P**	**this work**

REFERENCES

1. Chen, C.-X.; Wei, Z.-W.; Cao, C.-C.; Yin, S.-Y.; Qiu, Q.-F.; Zhu, N.-X.; Xiong, Y.-Y.; Jiang, J.-J.; Pan, M.; Su, C.-Y. All Roads Lead to Rome: Tuning the Luminescence of a Breathing Catenated Zr-MOF by Programmable Multiplexing Pathways. *Chemistry of Materials* **2019**, *31*, 5550-5557, doi:10.1021/acs.chemmater.9b01258.
2. Wang, X.; Que, M.; Chen, M.; Han, X.; Li, X.; Pan, C.; Wang, Z.L. Full dynamic-range pressure sensor matrix based on optical and electrical dual-mode sensing. *Adv. Mater.* **2017**, *29*, 1605817, doi:10.1002/adma.201605817.
3. Kim, G.; Cho, S.; Chang, K.; Kim, W.S.; Kang, H.; Ryu, S.P.; Myoung, J.; Park, J.; Park, C.; Shim, W. Spatially pressure-mapped thermochromic interactive sensor. *Adv. Mater.* **2017**, *29*, 1606120, doi:10.1002/adma.201606120.
4. Jia, C.; Xia, Y.; Zhu, Y.; Wu, M.; Zhu, S.; Wang, X. High-brightness, high-resolution, and flexible triboelectrification-induced electroluminescence skin for real-time imaging and human-machine information interaction. *Adv. Funct. Mater.* **2022**, *32*, 2201292, doi:10.1002/adfm.202201292.
5. Su, L.; Jiang, Z.; Tian, Z.; Wang, H.; Wang, H.; Zi, Y. Self-powered, ultrasensitive, and high-resolution visualized flexible pressure sensor based on color-tunable triboelectrification-induced electroluminescence. *Nano Energy* **2021**, *79*, doi:10.1016/j.nanoen.2020.105431.
6. Peng, M.; Li, Z.; Liu, C.; Zheng, Q.; Shi, X.; Song, M.; Zhang, Y.; Du, S.; Zhai, J.; Wang, Z.L. High-resolution dynamic pressure sensor array based on piezo-phototronic effect tuned photoluminescence imaging. *ACS Nano* **2015**, *9*, 3143-3150, doi:10.1021/acsnano.5b00072.
7. Wang, X.; Zhang, H.; Dong, L.; Han, X.; Du, W.; Zhai, J.; Pan, C.; Wang, Z.L. Self-powered high-resolution and pressure-sensitive triboelectric sensor matrix for real-time tactile mapping. *Adv. Mater.* **2016**, *28*, 2896-29903, doi:10.1002/adma.201503407.

8. Wang, Y.; Wang, H.L.; Li, H.Y.; Wei, X.Y.; Wang, Z.L.; Zhu, G. Enhanced high-resolution triboelectrification-induced electroluminescence for self-powered visualized interactive sensing. *ACS Appl. Mater. Interfaces* **2019**, *11*, 13796-13802, doi:10.1021/acsami.9b02313.
9. Lee, B.; Oh, J.Y.; Cho, H.; Joo, C.W.; Yoon, H.; Jeong, S.; Oh, E.; Byun, J.; Kim, H.; Lee, S.; et al. Ultraflexible and transparent electroluminescent skin for real-time and super-resolution imaging of pressure distribution. *Nat. Commun.* **2020**, *11*, 663, doi:10.1038/s41467-020-14485-9.
10. Wang, H.; Wang, W.; Kim, J.J.; Wang, C.; Wang, Y.; Wang, B.; Lee, S.; Yokota, T.; Someya, T. An optical-based multipoint 3-axis pressure sensor with a flexible thin-film form. *Sci. Adv.* **2023**, *9*, eadi2445, doi:10.1126/sciadv.adi2445.
11. Jang, J.; Kim, H.; Ji, S.; Kim, H.J.; Kang, M.S.; Kim, T.S.; Won, J.E.; Lee, J.H.; Cheon, J.; Kang, K.; et al. Mechanoluminescent, air-dielectric MoS_2 transistors as active-matrix pressure sensors for wide detection ranges from footsteps to cellular motions. *Nano Lett.* **2020**, *20*, 66-74, doi:10.1021/acs.nanolett.9b02978.
12. Jang, J.; Ji, S.; Grandhi, G.K.; Cho, H.B.; Im, W.B.; Park, J.U. Multimodal digital X-ray scanners with synchronous mapping of tactile pressure distributions using perovskites. *Adv. Mater.* **2021**, *33*, 2008539, doi:10.1002/adma.202008539.
13. Bao, R.; Wang, C.; Dong, L.; Shen, C.; Zhao, K.; Pan, C. CdS nanorods/organic hybrid LED array and the piezo-phototronic effect of the device for pressure mapping. *Nanoscale* **2016**, *8*, 8078-8082, doi:10.1039/c6nr00431h.
14. Wu, Z.; Chen, S.; Fan, S.; Qiao, Z.; Qi, J.; Zhang, Y.; Lim, C.T. Strain-localized luminescent e-skin for high-resolution pressure mapping and visual force feedback. *Nat. Commun.* **2026**, doi:10.1038/s41467-026-73073-5.